

CLASSIFICATION OF MINERAL INCLUSIONS IN ANCIENT CERAMICS: COMPARING DIFFERENT MODAL ANALYSES STRATEGIES

ABSTRACT

Digital image analysis has recently emerged as a powerful tool for the analysis of the ceramic thin sections. By producing quantitative data, it increases the usefulness of ceramic petrography to address archaeological questions. Despite several works considering digital image analysis to study archaeological ceramic materials, so far no work has been proposed to evaluate the possibilities of optical microscopy (OM) image analysis for classification and modal analysis, knowing its advantages and drawbacks, as compared to scanning electron microscopy (SEM) image processing. In this work we propose an algorithm to count the mineral inclusions correctly classified by OM image analysis with respect to SEM images. The proposed algorithm is based on a matching mechanism applied to the regions of interest (ROIs) detected in the OM images according to the corresponding ROIs as detected in the SEM images. Moreover, a comparison with point counting on the same OM images is also provided to evaluate the pros and cons of each method. Two Holocene potsherds (8900-4200 BP) are considered as case study for modal analysis to identify and classify quartz, feldspars and carbonate aggregates as mineral inclusions.

KEYWORDS: ceramics, optical microscopy, image processing, scanning electron microscopy , point counting, thin sections, classification of mineral inclusions.

1. INTRODUCTION

Point-counter and visual estimation charts have been usually used in petrography to perform quantitative investigations via thin section that is to provide modal estimation and identification of mineralogical phases as well as semi-quantification of their morphometry and texture (Chayes, 1954; Powers, 1963; Van der Plas and Tobi, 1965; DeHoff and Rhines, 1968; Howarth, 1998). Since these practices may be subjective and time-consuming, digital image analysis techniques were proposed to automatize the work. In this way a set of parameters (like grain-size and shape descriptors) can be easily measured by using a digital image of the interested sample as acquired by sediment or rock thin sections (Perring et al., 2004; Smith and Beermann, 2007; Holden et al., 2009).

1 To perform image analysis, both optical and high-resolution images captured respectively by optical microscopy (OM)
2 and by scanning electron microscopy (SEM) are typically used for petrography purposes. However, the definition of
3 standardized procedures for image segmentation may be sometimes a challenging task in case of images captured by
4 OM because of similar optical properties shared by some minerals. Actually, ad-hoc strategies have to be defined in
5 order to properly isolate the mineralogical phases of interest ((Starkey and Samantaray, 1993; Fueten, 1997;
6 Heilbronner, 2000; Wilson et al., 2007; Izadi et al., 2015). Conversely, high-resolution images acquired by SEM, like
7 backscattered electrons ones (BSE), especially when coupled with X-ray chemical maps, generally may provide a
8 clearer contrast between some minerals or phases, providing thus for a straightforward identification also as it concerns
9 finer grains or minerals sharing similar chemical composition (Stutzman, 2004; Prakongkep et al. 2010; Prêt et al.
10 2010). On the other hand, the analysis of optical images provides a lot of advantages with respect to SEM. Firstly, it
11 may provide a wider array of discriminant features about mineralogical phases of interest (e.g. identify polymorphs,
12 distinguish crystals in monomineralic rock fragments, etc). Secondly, the image acquisition phase in OM is a low-cost
13 approach both in terms of sample preparation time and instrumentation used. Lastly, its flexibility may grow if an image
14 analysis freeware software is coupled with. Thin section petrography is also widely used to study ceramic
15 archaeological materials as one of the routine analytical techniques of ceramic petrography aimed to describe and
16 classify pottery fabric namely the mineralogical composition, percentage, shape, grain-size and orientation of
17 argillaceous minerals, non-plastic inclusions and pores (Shepard, 1956; Rice, 1987; Reedy, 2008; Peterson, 2009). As
18 ceramic petrography moved towards a more quantitative approach for textural analysis (Stoltman, 1989) and along with
19 the contemporary diffusion and improvement of digital devices, image analysis emerged as a powerful tool also for the
20 analysis of ceramic thin sections (Reedy, 2006). Pilot studies in the field are the ones by Middleton et al. (1985) and
21 Whitbread (1991) who respectively evaluated different strategies to perform point counting and to automatize its
22 procedures adopting the earliest proofs of digitalized images of ceramic thin sections. Later, Livingood and Cordell
23 (2009) evaluated and compared the accuracy and feasibility of digital image techniques against point counting using
24 digital images acquired by scanner. More recently, Reedy et al. (2014) presented an experimental work aimed to test the
25 consistency and reproducibility of image analysis in order to manage even more complex archaeological samples. They
26 finally stated that image analysis, by producing quantitative data, increases the usefulness of ceramic petrography to
27 address archaeological questions. Actually, the pieces of information that can be collected, especially about grain-size
28 and morphometry of mineral inclusions and their identification, allow to define raw material sources and provenance
29 and to reconstruct technological processes of production (Maggetti, 1982; Tite, 2008). In the last years, even more
30 works considered routinely digital image analysis to study archeological ceramic materials (e.g. Knappett et al., 2011;
31 Aprile et al., 2014; Dal Sasso et al., 2014; Eramo et al. 2014; Lopez et al., 2015; Thér, 2016). However, to our
32
33
34
35
36
37
38
39
40
41
42
43
44
45
46
47
48
49
50
51
52
53
54
55
56
57
58
59
60
61
62
63
64
65

1 knowledge, at present no work is known in the field which is aimed to evaluate the possibilities of OM image analysis
2 for classification and modal analysis, knowing its advantages and drawbacks, as compared to SEM image processing.
3
4 To such a purpose, in this work a classification strategy was developed to count the mineral inclusions correctly
5 classified by OM image analysis. Each class (e.g. one type of mineral inclusion) and the corresponding mineral
6 inclusions detected as regions of interest (ROIs) by segmentation of the OM images were compared with the ROIs
7 segmented in the corresponding SEM images, to evaluate the accuracy of the classification obtained with the OM image
8 analysis. To do this, ad-hoc image segmentation procedures were firstly assessed for both OM and SEM images in order
9 to isolate and recognize the considered mineral inclusions. Then, an algorithm was proposed to classify automatically
10 the ROIs detected in the OM images according to the corresponding ROIs as detected in the SEM images. Moreover, a
11 comparison with point counting on the same OM images is also provided. The paper is organized as follows. In section
12 1 the state of the art and the adopted workflow are summarized, as seen. In section 2 the image acquisition phase
13 (section 2.1) is described and the image segmentation strategy (section 2.3) adopted for both OM and SEM images and
14 eventually the rectification phase required after image segmentation (section 2.4). The algorithm developed to classify
15 the ROIs detected in the OM images according to the corresponding ROIs as detected in the SEM images is then
16 formalized (section 2.5). Modal analysis as performed by point counting is also described here (section 2.2).
17 Classification performance observed is hence evaluated and discussed in sections 3 and 4.

31 2. Materials and Methods

32 carbonate According to the aim of the work, the selected techniques for modal analysis were applied to two Late Acacus
33 potsherds (8900-4900 BP) which were chosen as case study according to their simpler mineral composition that is
34 prevalent quartz, feldspars and carbonate aggregates as mineral inclusions (Figure 1). These samples are a part of a
35 larger selection of representative potsherds belonging to the Takarkori rock-shelter archaeological site (Libyan Sahara),
36 as described in Eramo et alii (2014). According to this study, the selected samples may be thus considered reliable for
37 the estimation of the real mineral composition of such ceramics.

38 In this work, two types of images particularly were manipulated:

- 39 1) OM images composed by pairs of plane (P) and cross (XP) polarized light images (used for both optical image
40 analysis and point counting);
- 41 2) X-ray elemental maps produced by SEM/EDS.

42 In the following the acquisition of these images is described.

2.1. Image Acquisition

Image acquisition of optical images considered four pairs of P and XP images in RGB digital format (resolution of 1920x2560 pixel size) acquired in transmitted light for each thin section at a magnification of 2.5x (1.315 mm/pixel) as shown in Figure 2. The four different areas maintain a distance of 1 cm between the center of each frame by the successive one and moving lengthwise on the thin section. A ZEISS Axioskop 40 Pol optical microscope for petrography, equipped with a Nikon DS-5MC digital camera with 2/3" CCD (Peltier cooling system), was used to such a purpose.

By using SEM, backscattered (BSE) images (resolution of 4096x3328 pixel size) and the associated set of elemental X-ray maps of Al, Ca, Fe, Si, K, Mg, P, Na and Ti (resolution of 2046x1664 pixel size) corresponding to the same areas considered for optical microscopy acquisition were acquired from each sample at a magnification of 65x (Figure 3). A ZEISS LEO 50XVP scanning electron microscope, operated at 15 kV, equipped with a X-MaxN80mm² SDD detector and Aztec software (Oxford Instruments) for X-ray maps was used.

2.2. Point Counting

To perform modal analysis via point counting (PC), the point counter tool of the freeware software *JMicroVision* (Roduit, 2017) has been adopted, which allows the operator to obtain automatic statistics (i.e. frequency and volume) of phases of interest recognized during the eye-naked identification step. A total of 1200 points per thin section (300 per area) were counted using the four pairs of P-XP images acquired by OM. Particularly, only the considered mineral inclusions of quartz, feldspars and carbonate aggregates were counted, in order to normalize the tallies among areas and make a sound comparison with the same corresponding inclusions as segmented by OM and SEM images (see section 2.3). The accuracy of the percentages obtained by point counting was calculated after Howarth (1998).

2.3. Image Segmentation

The segmentation phase was devoted to isolate ROIs of the three considered types of mineral inclusions by manipulating the acquired OM and SEM images to produce corresponding binary images. To such a purpose, different segmentation procedures for the two types of images were developed, as described in the following.

2.3.1. Optical Microscopy

1
2 For quartz and carbonate aggregates we adopted the image segmentation procedure based on mathematical operators as
3 described in Aprile et al. (2014). To succeed in feldspars segmentation (i.e. to separate individual grains), it has been
4 primarily considered that, according to their optical similarity, the twinning phenomena may be useful to distinguish
5 between quartz and feldspars (Edwards, 2008). In these samples it has been particularly observed that twinned regions
6 were characterized by different texture with respect to quartz because of their altered nature. To such a purpose, the P
7 images were manipulated in order to define an ad-hoc segmentation strategy because they showed more clearly the
8 outlines of interested regions (Aprile et al., 2014). Particularly, the *K-means clustering* algorithm (Jain and Dubes,
9 1988) implemented in *ImageJ* (Ferreira and Rasband, 2010-2012) was applied to P images. As described in Aprile et al.
10 (2014) for the other procedures adopted, corresponding binary images of quartz and carbonate aggregates were inverted
11 and filtered using the *Gaussian Blur*, the *Median* and the *Maximum* filters in order to guarantee a better overlap of the
12 edges with the P image in the next steps. Actually, these images were subtracted by the P image previously processed.
13 Then, in order to obtain the binary image containing ROIs of the class of feldspars, we finally applied the *Isodata*
14 thresholding method and the median filter *Despeckle* to reduce noise. Both methods are implemented in *ImageJ*. Figure
15 4 summarizes the segmentation procedure adopted for quartz, carbonate aggregates and feldspars in the case of OM
16 images, showing an example of the corresponding binary images produced.
17
18
19
20
21
22
23
24
25
26
27
28
29
30
31
32
33
34
35

2.3.2. Scanning Electron Microscopy

36
37
38 To perform segmentation the elemental maps of Si, Ca, Na and K were selected because they are considered more
39 informative, on the base of their chemical composition, to identify our mineralogical phases of interest. Then, each map
40 was assigned to a channel in the visible band (i.e. Red = map of Si; Green = map of Ca+Na; Blue = map of K). The
41 freeware software for multispectral analysis Multispec © (Landgrebe and Biehl, 1991-2011) was used to such a
42 purpose. A multispectral image containing different areas corresponding to the phases of interest according to the
43 abundance/presence of those chemical elements in each phase. It must be specified that, even if the map of Na is usually
44 combined with the map of K to isolate alkali-feldspars, the map of K was used here on its own to such a purpose
45 because of the abundance of alkali-feldspars towards plagioclase. Rather, the combination of the maps of Na and Ca
46 (using the addition operator) worked out properly particularly to isolate carbonate aggregates and then plagioclase.
47 Similar strategies, which emphasize the chemical contribution of these elements, are also suggested by Lydon (2005).
48 Then, a supervised classification was applied by means of the training fields method (Lydon, 2005) as implemented in
49 Multispec © to automatically classify pixels of the multispectral image into the corresponding regions of quartz,
50
51
52
53
54
55
56
57
58
59
60
61
62
63
64
65

feldspars and carbonate aggregates (Fig. 5). By adopting this method, it is known where all mineral classes occur in the image and hence the user can manually select corresponding areas to be used as training examples. Particularly, thirty areas per phase were selected. In order to obtain the corresponding binary images, the *Isodata* thresholding method and the median filter *Despeckle* to reduce noise (Fig. 6) were finally applied. Moreover, SEM binary images were resized according to the resolution of OM images.

2.4. Rectification phase

To correctly apply the proposed classification strategy (see section 2.5), it is necessary that pairs of corresponding ROIs of OM and SEM binary images overlap as much as possible. Since they are obtained using two different acquisition instrumentations, it is natural to have topological differences between pairs of corresponding OM and SEM images even if acquired from the same area. Hence a geometric correction called rectification (simultaneous rotation and translation) was applied. To such a purpose, the *affine transformation* method (Jain, 1986) was applied, a linear mapping method preserving points, straight lines and planes so that sets of parallel lines remain the same after its application. The JMicroVision tool was used, which applies the affine transformation on the basis of at least three control points applied on one image that will be also visualized in the corresponding image to be rectified. Particularly, each SEM binary image was rectified by selecting fifty control points per corresponding OM binary image. The corresponding control points on SEM binary image were then shifted manually until a match of corresponding ROIs in both images was achieved. Actually, each pair of control points must match eventually the same location on both images as much as possible to achieve accurate geometric correction. Effects of rectification phase on OM and SEM binary images are shown in Figure 7.

2.5. Counting correctly classified ROIs in OM images

The algorithm developed to perform automatic counting of the correctly classified ROIs of OM images previously segmented is provided as Supplementary material.

3. RESULTS

In the modal analyses carried out with PC we considered grain-size above 16 μm , which approximates, according to the scale of Udden-Wentworth (1922), the limit of 15 μm to define the non-plastic inclusions (NPIs) of the ceramic body proposed by Maggetti (1982). PC was carried out on the same four areas of samples TK66 and TK69 chosen for image analysis. In both samples it was observed that quartz is the prevalent phase among those counted, while the relative amounts of feldspars and carbonate aggregates are inverted (Table 1). Moreover, if the variability of data among areas of the same sample is considered, sample TK69 shows higher heterogeneity. The relative standard deviation (RSD) of the points counted per mineral phase ranges from 0.08 to 0.57 in TK66 and from 0.18 to in TK69. Quartz has the lowest RSD values in both samples. Consequently, it can be said that the sample TK66 is relatively rich in feldspars, while quartz and carbonate aggregates prevail in the sample TK69.

According to Table 2, the size distribution of the ROIs with grain-size above 16 μm is unimodal in both SEM and OM images. While the frequency mode for the SEM ROIs is in the range 16-32 μm , a shift in the range 32-63 μm is observed for the OM ROIs.

As it concerns the evaluation of image analysis results, it was chosen to define a grain-size threshold value α based on maximum Feret diameter (extracted by using the *ImageJ* tool) in order to allow accurate comparison between corresponding detected ROIs of OM and SEM identified after segmentation. Actually, SEM enables a better detection of mineral phases for the smaller grain-sizes than OM, leading typically to a larger number of detected ROIs that is $N \gg M$ (see also section 4). This can be clearly observed in Table 2, where the number of quartz OM ROIs are generally only half of the ROIs segmented in SEM images. Conversely, for feldspars and calcite aggregates the ROIs segmented in OM images are down to a tenth of those in SEM images. Particularly, the larger number of detected SEM ROIs is observed in the range 16-32 and 32-63 μm as expected. Only in TK69, calcite aggregates detected in OM images are overestimated in this grain-size ranges. It was then defined $\alpha = 63\mu\text{m}$ as lower threshold for our analysis. Actually, this limit provides the best compromise according to grain-size range generally observed for mineral inclusions in ancient ceramics when adopting both OM and SEM. Three different grain filtering approaches were consequently applied, to obtain ROIs characterized by three grain-sizes according to Feret value: (a) larger than 63 μm ; (b) larger than 125 μm and (c) larger than 250 μm . Table 3 shows the number M and N respectively of ROIs in the OM and ROIs in the SEM segmented images for the considered three grain-sizes for quartz, feldspars and carbonate aggregates, and highlights how the grain size thresholding affects the modal analysis. It can be seen that quartz and carbonate aggregates show almost similar values of M and N, while in the case of feldspars the values of N are higher than M, particularly for the grain-size including the finer fraction corresponding to Feret > 63 μm .

1
2
3
4
5
6
7
8
9
10
11
12
13
14
15
16
17
18
19
20
21
22
23
24
25
26
27
28
29
30
31
32
33
34
35
36
37
38
39
40
41
42
43
44
45
46
47
48
49
50
51
52
53
54
55
56
57
58
59
60
61
62
63
64
65

Next, for each considered grain-size of each class, it was applied the algorithm described in section 2.5 to count the number p of correctly classified ROIs in the OM segmented images namely the matching pairs (A_i, B_j) . The classification accuracy was then calculated as:

$$ACC = p/M$$

In this way, the reliability of our OM image segmentation was evaluated in identifying the mineral inclusions of interest in comparison to the classification achieved via SEM image analysis, which is considered as a ground truth. Results are shown in Figure 8. It can be observed that generally the classification accuracy increases according to grain-size and it is higher for all ROIs having Feret greater than 250 μm . Only for carbonate aggregates the classification accuracy slightly decreases for grain-size greater than 250 μm . Moreover, it can be seen that the classification accuracy in the case of feldspars is the highest among the considered classes.

4. DISCUSSION AND COMPARISON

The three different approaches to modal analysis namely PC, OM and SEM image analysis, applied to the same areas of the two ancient potsherds investigated, show uneven results and give thus room to several discussion points summarized in the following. The classification accuracy (ACC) of image analysis was based on frequency of ROIs estimated by the differences between OM percentage and SEM percentage. Particularly, it was observed that ACC generally gets higher when grain-size increases. This may depend on OM limitation which deals with masking finer NPIs with respect to SEM, effect due to (a) the different image aberrations of transmitted light microscopy and (b) the different characters of sectioning even though thin sections are used in both cases. Actually, when a thin section of pottery or finegrained material is observed by OM in transmitted light, a masking effect due to the overlapping of particles whose Feret is less than 30 μm is more probable. It follows that two or more features can appear to be a single one and a more or less opaque matrix can mask finer particles (Chayes, 1956). In SEM images conversely, thin section thickness does not influence image quality and contrast between grains and matrix is moreover improved by BSE and X-ray maps. The segmented particles in SEM images with Feret comprised between 16 μm and 63 μm are hence strongly masked in OM images, as just seen in Table 2. Moreover, when a cut is made in a granular solid material, the size and shape of particles is distorted. It is known that the average size of the grain sections will be less than the average size of the grains, since random sections through the grain along plain containing the maximum diameter is less probable (Krumbein, 1950). Moreover, the theoretical assumption of random distributed spheres within the sample is not wholly satisfied in fine-grained rocks, since they tend to be polymineralic, poorly sorted, and consist of grains with low

sphericities. The use of maximum Feret in sectioned grains is the best approximation to true intermediate axis of the whole grain, for both theoretical and practical reasons (Kellerhals et al., 1975). For the analyzed samples, the distortion of a given OM ROI area in respect to the corresponding ROI of SEM image was defined using the ratio A_{OM}/A_{SEM} in Figure 9. Different trends for carbonate aggregates and quartz and feldspars were found. Particularly, the carbonate aggregates are microcrystalline and appear more opaque than quartz and feldspars and show higher area distortion (>1), especially for finer particles. Although quartz and feldspars show a similar trend, the distortion of ROIs with Feret $> 63\mu\text{m}$ appeared somewhat bimodal. These transparent NPIs may be spherical zones of one or two bases immersed in a more or less opaque matrix. Just as a spherical zone of one base will give an OM ROI area smaller than the corresponding SEM ROI, a spherical zone of two bases will give a larger OM ROI area of that of SEM only if the smaller base of the grain is on the top the thin section. Being constant the geometry of the spherical zone, the A_{OM}/A_{SEM} ratio increase as the opacity of the matrix decreases. The strongest bias are produced by the finest fraction considered namely $63\text{-}125\mu\text{m}$. Such overestimation of area measurement is due to the Holmes effect (Cahn, 1959). Since the observation does not only involve a single plane, but a thin slice, the observations in transmitted light may produce an enlarged projection of the particle on the image plane of the microscope, leading to an overestimate of the area and the volume fraction of a given particle. This effect increases with opacity and with the smaller size of particles present in the thin section, partially or not sectioned. The marked magnification observed in the calcite aggregate ROIs segmented in TK69 may be due to the merging of several particles occurring at different height in the thin section. Rather SEM images prevent Holmes effect and are not affected by masking effect for finer grains. At low magnification (30-100x), they may suffer peripheral area distortion which can be attenuated increasing the number of sampling areas at higher magnification (e.g. 100-500x) or changing the electron beam characteristics. The bias observed in the finer grain-sizes between OM and SEM ROIs was eventually eliminated considering Feret values greater than $250\mu\text{m}$. This let to define a dimensional lower limit of grains segmented or counted on OM images for a more accurate modal analysis. Actually, while an upper limit of coarseness, expressed by the ratio of grain-section area to measurement area (Eramo et al., 2014), is important to define textural and compositional representativity of thin section in respect to hand specimen, the definition of an accurate lower limit may solve the difficulty to detect and evaluate the finer particles, which introduce systematic biases. The definition of the lower limit of coarseness for modal analysis at $63\mu\text{m}$ as done may represent a partial solution to this problem (Stoltman, 1989), even if the meaning of NPIs in the ceramic fabric may be distorted. Precisely, the grain-size threshold at $15\mu\text{m}$ (Maggetti, 1982), that separate the matrix from the NPIs in the ceramic fabric, cannot be used quantitatively when transmitted light microscopy is considered and the mode of the NPIs is below $63\mu\text{m}$. To be too selective (lower limit too high) may cause a lack of information especially for the less compositionally mature NPIs. In order to guarantee reproducibility and accuracy of the modal analysis, the image

1 acquisition conditions must be as closely controlled as possible, as well as the processing and measurements done on
2 images from both OM and SEM. Another limitation of OM observations deals with the identification of feldspars. As
3 explained in section 2.3.1, only the twinning occurrence may be really useful to such a purpose as well as to distinguish
4 between quartz and feldspars. It is obvious that SEM, especially when coupled with X-ray chemical mapping,
5 succeeded better in recognizing feldspars, since $N > M$ for feldspars was observed. However, it must be highlighted
6 that classification accuracy achieved by OM image analysis for feldspars was the highest among the considered classes.
7 Thus, the segmentation procedure on OM image for this class can be considered reliable. In addition, since the
8 percentage of correct classification of feldspars with OM image analysis is generally higher than the percentage
9 obtained with PC (without etch and/or stain thin sections) our approach seems to be an easy and cheap analytical
10 strategy to improve the petrographical analysis qualitatively and quantitatively. When PC data are compared to OM and
11 SEM data, more than one point counted may correspond to one ROI. Further, the number of points counted in each of
12 the four sampling areas per thin section partially covers the image, and the classification accuracy cannot be calculated
13 in the same manner as for image analysis. To ensure the percentages of quartz, feldspars and calcite aggregates to be
14 within a fixed accuracy, it was decided the number of points counted in order to obtain an uncertainty range of about 2
15 % for component percentages (Howarth, 1998). Further, it was observed that the accuracy of OM ROIs and PC is
16 affected by the grain-size distribution. The lower the grain-size, the higher the masking effect and the bias of optical
17 features of the grains. It should be further considered that in compositionally immature ceramic fabrics - thus in raw
18 materials - the mineralogical composition changes with the grain-size, and the variation of composition associated with
19 the lower limit of coarseness adopted should not be confused with the classification accuracy.
20
21
22
23
24
25
26
27
28
29
30
31
32
33
34
35
36
37
38
39
40
41

42 5. CONCLUSIONS

43
44 The differences between the OM and PC classification accuracy with reference to the ROIs segmented in the SEM
45 images, put in evidence the limits of OM to objectively classify NPIs in thin section and their effect on modal analysis.
46 If on one hand the analytical error increases as the number of particles sectioned in the measurement area decreases, on
47 the other hand the less the ratio between the particle diameter and the thin section thickness, the more the systematic
48 biases affecting the results (Chayes, 1956). Our results show that even when a lower limit of coarseness at $250\mu\text{m}$ is
49 applied, OM and PC results do not match the SEM results. Most of the particles with Feret $< 63\mu\text{m}$ were not detected in
50 OM images and classification errors were more frequent. However, feldspars identification by image analysis resulted
51 more accurate than that by petrographic observation. On fine-grained crystals, where the optical features of different
52 feldspars are less detectable under the polarizing microscope, the feldspars segmentation here proposed is a useful tool
53
54
55
56
57
58
59
60
61
62
63
64
65

1 to improve the accuracy of modal analysis obtained from OM analysis. If the rise of the lower limit of coarseness
2 improve the classification accuracy, it could "hide" some important components of the ceramic fabric. When a limit is
3 set, it should be used for all the investigated samples in order to spread the same compositional bias related to grain-size
4 filtering, and then to make comparable quantitative results otherwise not comparable. Eventually it can be asserted that,
5 given SEM-based modal analysis as ground truth, modal analysis via OM and/or PC may be considered with a
6 magnitude of uncertainty that can be tolerated according to research aims and experimental design adopted.
7

8
9
10
11
12 In this row, the accuracy tests on ceramics will be extended to more complex textures and petrographical compositions
13 to further improve the recognition and separation of minerals in digital images. Such results will help to better
14 understand the pros and cons of promote the use of quantitative petrography via digital image analysis and its potential
15 as complementary method in archaeometry for ceramics analysis.
16
17
18
19
20
21
22
23

24 Acknowledgements

25
26
27 The authors thank Pasquale Acquafredda and Nicola Mongelli for their technical support in SEM analysis. Special
28 thanks are also due to Lara Maritan for her fruitful suggestions on the processing of the elemental maps. This research
29 benefited of instrumental upgrades of Potenziamento Strutturale PONA3-00369 dell'Università degli Studi di Bari Aldo
30 Moro titled "Laboratorio per lo Sviluppo Integrato delle Scienze e delle TECnologie dei Materiali Avanzati e per
31 dispositivi innovativi (SISTEMA)".
32
33
34
35
36
37
38
39
40

41 References

- 42
43 Aprile A, Castellano G, Eramo G (2014) Combining image analysis and modular neural networks for classification of
44 mineral inclusions and pores in archaeological potsherds. *J Archaeol Sci* 50:262-272.
45
46 Chayes F (1954) The theory of thin-section analysis. *J Geol* 62:92-101.
47
48 Chayes F (1956) *Petrographic Modal Analysis*. John Wiley and Sons, New York.
49
50 Cahn JW (1959) A Quantitative Correction for the Holmes Effect. *Am Mineral* 44:435-437.
51
52 Dal Sasso G, Maritan L, Salvatori S, Mazzoli C, Artioli G (2014) Discriminating pottery production by image analysis:
53 a case study of Mesolithic and Neolithic pottery from Al Khiday (Khartoum, Sudan). *J Archaeol Sci* 46:125-143.
54
55 DeHoff RT, Rhines FN (1968) *Quantitative microscopy*. Mc Graw Hill, New York.
56
57 Eramo G, Aprile A, Muntoni IM, Zerboni A (2014) Textural and morphometric analysis applied to Holocene pottery
58 from Takarkori rock shelter (SW Libya, Central Sahara): a quantitative sedimentological approach. *Archaeometry* 56
59 (Suppl. 1):36-57.
60
61 Fueten F (1997) A computer-controlled rotating polarizer stage for the petrographic microscope. *Comput Geosci*
62 23:203-208.
63
64
65

- 1 Ferreira T, Rasband WS (2010-2012) ImageJ User Guide - IJ 1.46. <http://imagej.nih.gov/ij/docs/guide/>. Accessed
2 December 2016.
- 3 Francus P (1998) An image-analysis technique to measure grain-size variation in thin sections of soft elastic sediments.
4 *Sediment Geol* 121:289-298.
- 5 Holden EJ, Moss S, Russell JK, Dentith MD (2009) An image analysis method to determine crystal size distributions of
6 olivine in kimberlite. *Comput Geosci* 13:255-268.
- 7
8 Howarth RJ (1998) Improved estimators of uncertainty in proportions, point counting, and pass-fail test results. *Am J*
9 *Sci* 298:594-607.
- 10 Heilbronner R (2000) Automatic grain boundary detection and grain size analysis using polarizing micrographs or
11 orientation image. *J Struct Geol* 22:969-981.
- 12
13 Izadi H, Sadri J, Mehran NA (2015) A new intelligent method for minerals segmentation in thin sections based on a
14 novel incremental color clustering. *Comput Geosci* 81:38-52.
- 15
16 Jain A (1986) *Fundamentals of digital image processing*. Prentice-Hall.
- 17
18 Kellerhals R, Shaw J, Arora VK (1975) On grain size from thin sections. *J Geol* 83:79-96.
- 19
20 Knappett C, Pirrie D, Power MR, Nikolakopoulou I, Hilditch J, Rollinson GK (2011) Mineralogical analysis and
21 provenancing of ancient ceramics using automated SEM-EDS analysis (QEMSCANR): a pilot study on LB I pottery
22 470 from Akrotiri, Thera. *J Archaeol Sci* 38:219-232.
- 23
24 Landgrebe D, Biehl L (1991-2011) *An Introduction & Reference For MultiSpec® Version 9.2011*.
25 <https://engineering.purdue.edu/biehl/MultiSpec/>. Accessed April 2016.
- 26
27 Livingood PC, Cordell AS (2009) Point/counter point: the accuracy and feasibility of digital image techniques in the
28 analysis of ceramic thin section. *J Archaeol Sci* 36:867-872.
- 29
30 Lydon JW (2005) The measurement of the modal mineralogy of rocks from SEM imagery: the use of Multispec© and
31 ImageJ freeware. Geological Survey of Canada, Open File 4941.
- 32
33 Lopez P, Lira J, Hein I (2015) Discrimination of ceramic types using digital image processing by means of
34 morphological filters. *Archaeometry* 57:146-162.
- 35
36 Maggetti M (1982) Phase analysis and its significance for technology and origin. In: Olin GS, Franklin AD (eds)
37 *Archeological Ceramics*, Smithsonian Institution Press, Washington, pp 121-133.
- 38
39 Middleton AP, Freestone IC, Leese MN (1985) Textural analysis of ceramic thin sections: evaluation of grain sampling
40 procedures. *Archaeometry* 27:64-74.
- 41
42 Perring CS, Barnes SJ, Verrall M, Hill RET (2004) Using automated digital image analysis to provide quantitative
43 petrographic data on olivine-phyric basalts. *Comput Geosci* 30:183-195.
- 44
45 Peterson SE (2009) *Thin section petrography of ceramic materials*. INSTAP Archaeological Excavation Manual 2.
46 INSTAP Academic Press Philadelphia, Pennsylvania.
- 47
48 Powers MC (1953) A new roundness scale for sedimentary particles. *J Sediment Petrol* 23:117-119.
- 49
50 Prakongkep N, Suddhiprakarn A, Kheoruenromne I, Gilkes RJ (2010) SEM image analysis for characterization of sand
51 grains in Thai paddy soils. *Geoderma* 156:20-31.
- 52
53 Prêt D, Sammartino S, Beaufort D, Meunier A, Fialin M, Michot LJ (2010) A new method for quantitative petrography
54 based on image processing of chemical element maps, part I: mineral mapping applied to compacted bentonites. *Am*
55 *Mineral* 95:1379-88.
- 56
57 Reedy CL (2006) Review of Digital Image Analysis of Petrographic Thin Sections in Conservation Research. *J Am*
58 *Inst Conserv* 45:127-146.
- 59
60 Reedy CL (2008) *Thin section petrography of stone and ceramic cultural materials*. Plymouth, U.K.
- 61
62 Reedy C, Anderson J, Reedy T, Liu Y (2014) Image analysis in quantitative particle studies of archaeological ceramic
63 thin sections. *Adv Archaeol Prac* 2:252-268.
- 64
65

1 Rice MP (1987) Pottery analysis: a sourcebook. University of Chicago Press, Chicago.

2 Roduit N (2017) JMicroVision: Image analysis toolbox for measuring and quantifying components of high-definition
3 images. Version 1.2.7. <http://www.jmicrovision.com>. Accessed February 2017.

4 Shepard AO (1956) Ceramics for the Archaeologist. Carnegie Institution of Washington, Washington

5
6 Smith JV, Beermann E (2007) Image analysis of plagioclase crystals in rock thin sections using grey level homogeneity
7 recognition of discrete areas. Comput Geosci 33:335-356.

8
9 Smith CS, Guttman L (1953) Measurement of internal boundaries in three dimensional structures by random sectioning.
10 Trans Aime 197:81-87.

11 Starkey J, Samantaray AK (1993) Edge detection in petrographic images. J Microsc 172:263-266.

12
13 Stoltman JB (1989) A quantitative approach to the petrographic analysis of ceramic thin sections. Am Antiquity 54:147-
14 160.

15
16 Stutzman P (2004) Scanning electron microscopy imaging of hydraulic cement microstructure. Cement Concrete Comp
17 26:957-66.

18
19 Thér R (2016) Identification of pottery-forming techniques using quantitative analysis of the orientation of inclusions
20 and voids in thin sections. Archaeometry 58:222-238.

21
22 Textoris DA (1972) Grain-size measurement in thin-section. In: Carver RE, Douglas LA (eds) Procedures in
23 Sedimentary Petrology, Wiley-Interscience, New York, pp 95-107.

24
25 Tite MS (2008) Ceramic production, provenance and use-a review. Archaeometry 50:216-231.

26
27 Van der Plas L, Tobi AC (1965) A chart for judging the reability of point counting results. Am J Sci 263:87-90.

28
29 Wentworth CK (1922) A scale of grade and class terms for clastic sediments. J Geol 30 (5):377-392.

30
31 Whitbread IK (1991) Image and data processing in ceramic petrology. In: Middleton A, Freestone IC (eds) Recent
32 Developments in Ceramic petrology, British Museum Publications Ltd., London, pp 369-388.

33
34 Wilson CJL, Russell-Head DS, Kunze K, Viola G (2007) The analysis of quartz c-axis fabrics using a modified optical
35 microscope. J Microsc 227:30-41.

36 37 38 FIGURES:

39
40 Figure 1: Example of thin section of the potsherds considered as case study (unpolarized light).

41
42 Figure 2: Example of plane (P) and cross polarized (XP) light images acquired by optical microscopy (OM) in
43 transmitted light.

44
45 Figure 3: Example of backscattered (BSE) and corresponding elemental maps of Al, Ca, Fe, Si, K, Mg, P, Na and Ti
46 acquired by scanning electron microscopy (SEM/EDS).

47
48 Figure 4: Segmentation of OM images and corresponding binary images (Qtz = quartz; Feld = feldspars; Cal =
49 carbonate aggregates) produced via the *K-means* algorithm implemented in *ImageJ*.

50
51 Figure 5: Multispectral image of the selected SEM elemental maps as segmented by the training field method
52 implemented in Multispec©.

53
54 Figure 6:

55
56 Binary images of quartz, feldspars and carbonate aggregates as obtained by the multispectral image applied to SEM
57 elemental maps manipulated using *ImageJ* (Qtz=quartz; Cal=carbonate aggregates; Feld=Feldspars).

58
59 Figure 7: Rectification phase: a) Inaccurate overlap of corresponding OM and SEM binary images due to the different
60 acquisition instruments; b) Overlap of OM and SEM binary images after application of the affine transformation by
61 means of control points.

1
2
3
4
5
6
7
8
9
10
11
12
13
14
15
16
17
18
19
20
21
22
23
24
25
26
27
28
29
30
31
32
33
34
35
36
37
38
39
40
41
42
43
44
45
46
47
48
49
50
51
52
53
54
55
56
57
58
59
60
61
62
63
64
65

Figure 8: Classification accuracy as achieved by image analysis (Qtz = quartz; Feld = feldspars; Cal = carbonate aggregates).

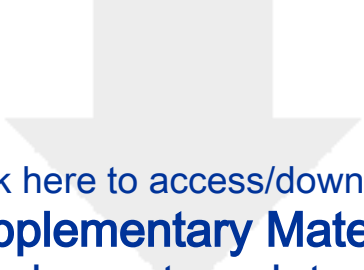
Figure 9: Area distortion corresponding to the three considered classes for sample TK66 (left side) and TK69 (right side). Mild outliers (1.5-3 IQR) are shown as circles, while extreme outliers (>3 IQR) are shown as stars.

TABLES:

Table 1: Statistics of PC and modal composition (percentage) for samples TK66 and TK69 (Qtz = quartz; Feld = feldspars; Cal = carbonate aggregates).

Table 2: Grain-size distribution as achieved by PC for samples TK66 and TK69 (Qtz = quartz; Feld = feldspars; Cal = carbonate aggregates).

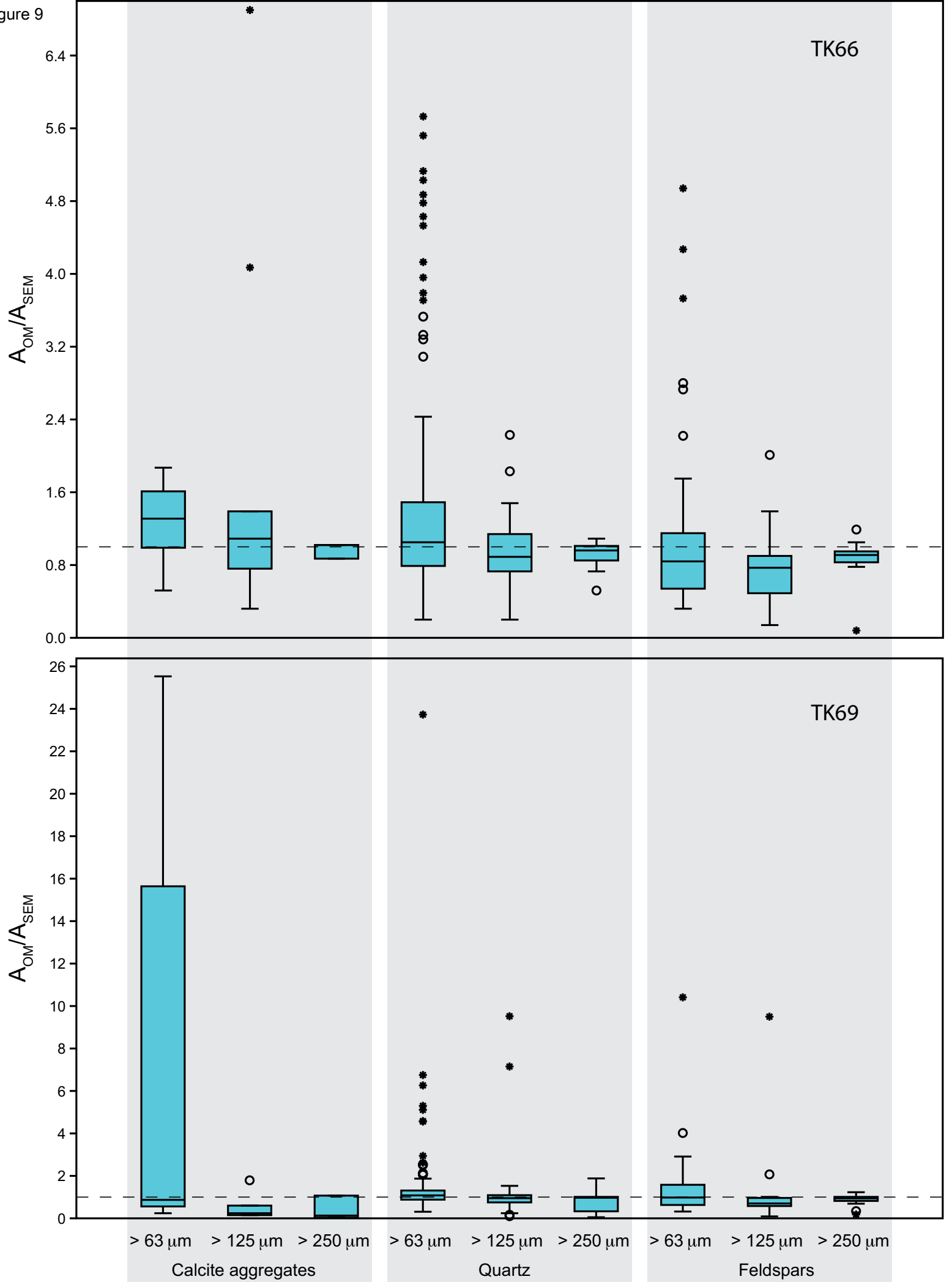
Table 3: Number of OM (M) and SEM (N) ROIs as detected by the segmentation phase for each considered grain-size



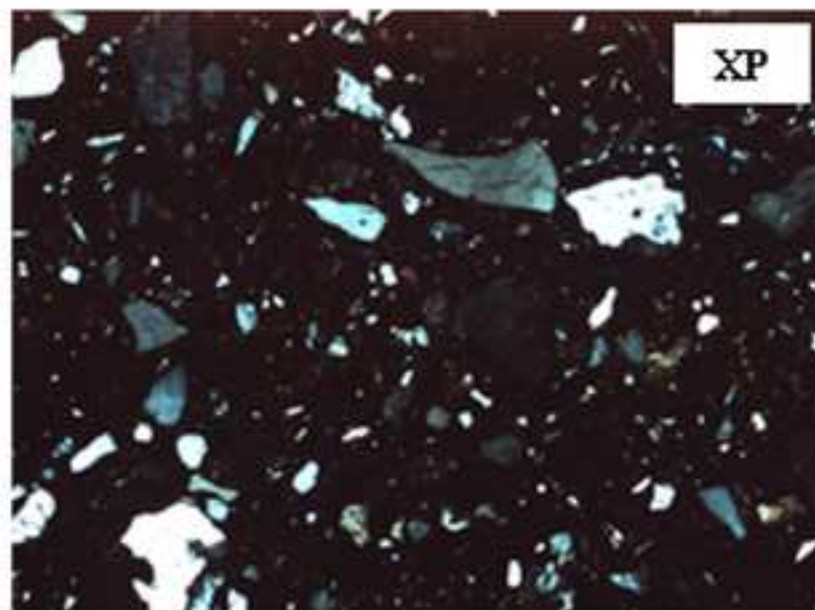
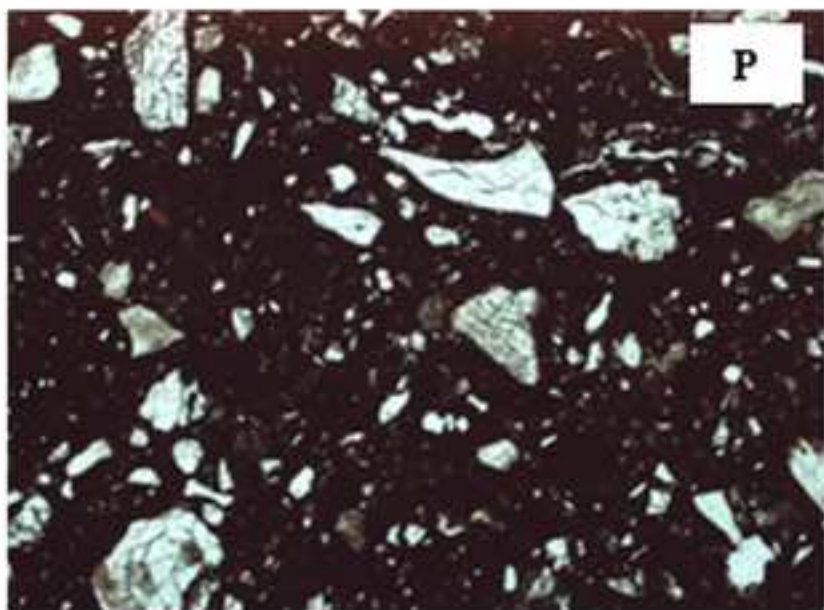
Click here to access/download
Supplementary Material
supplementary data.doc

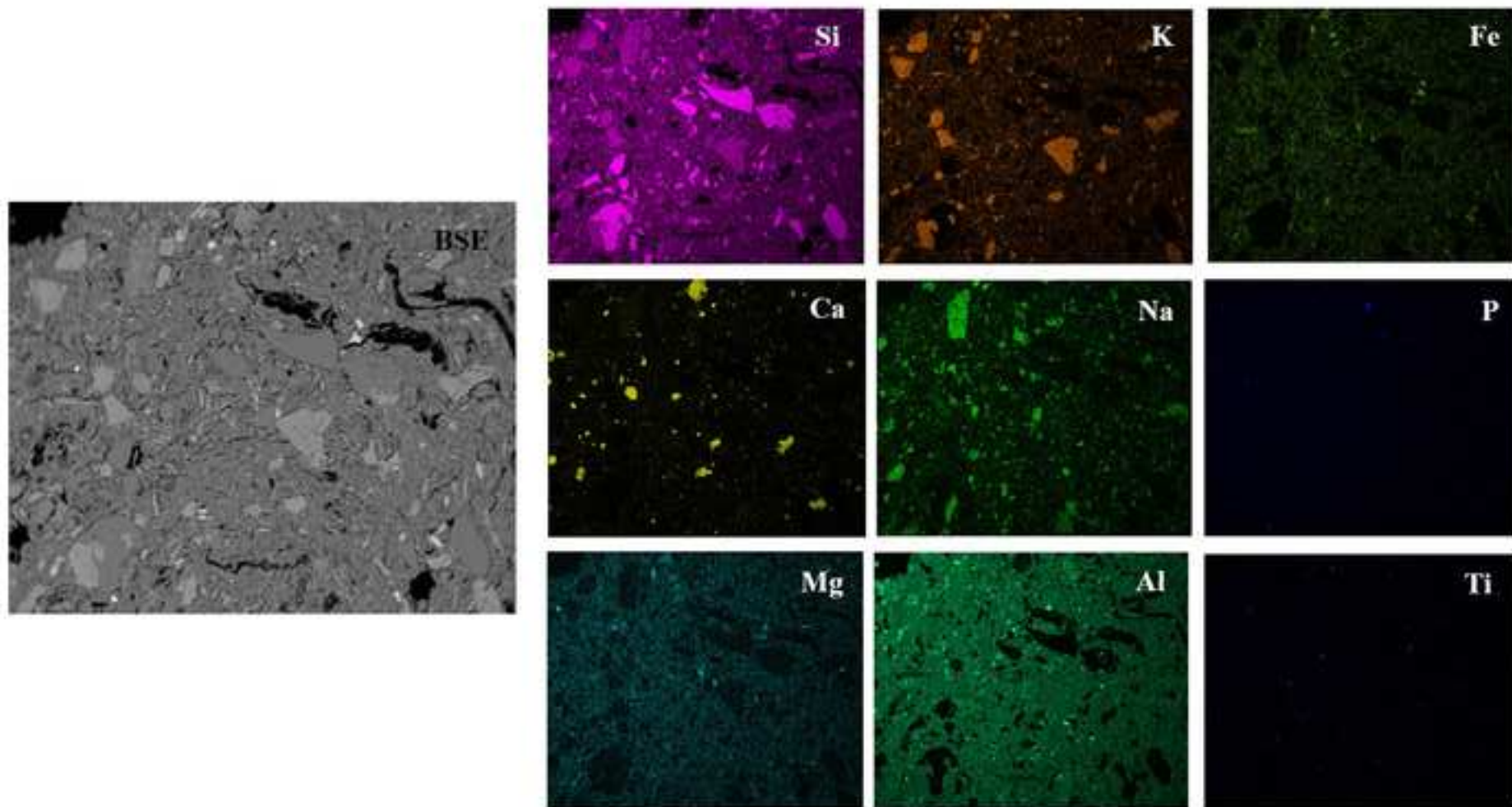


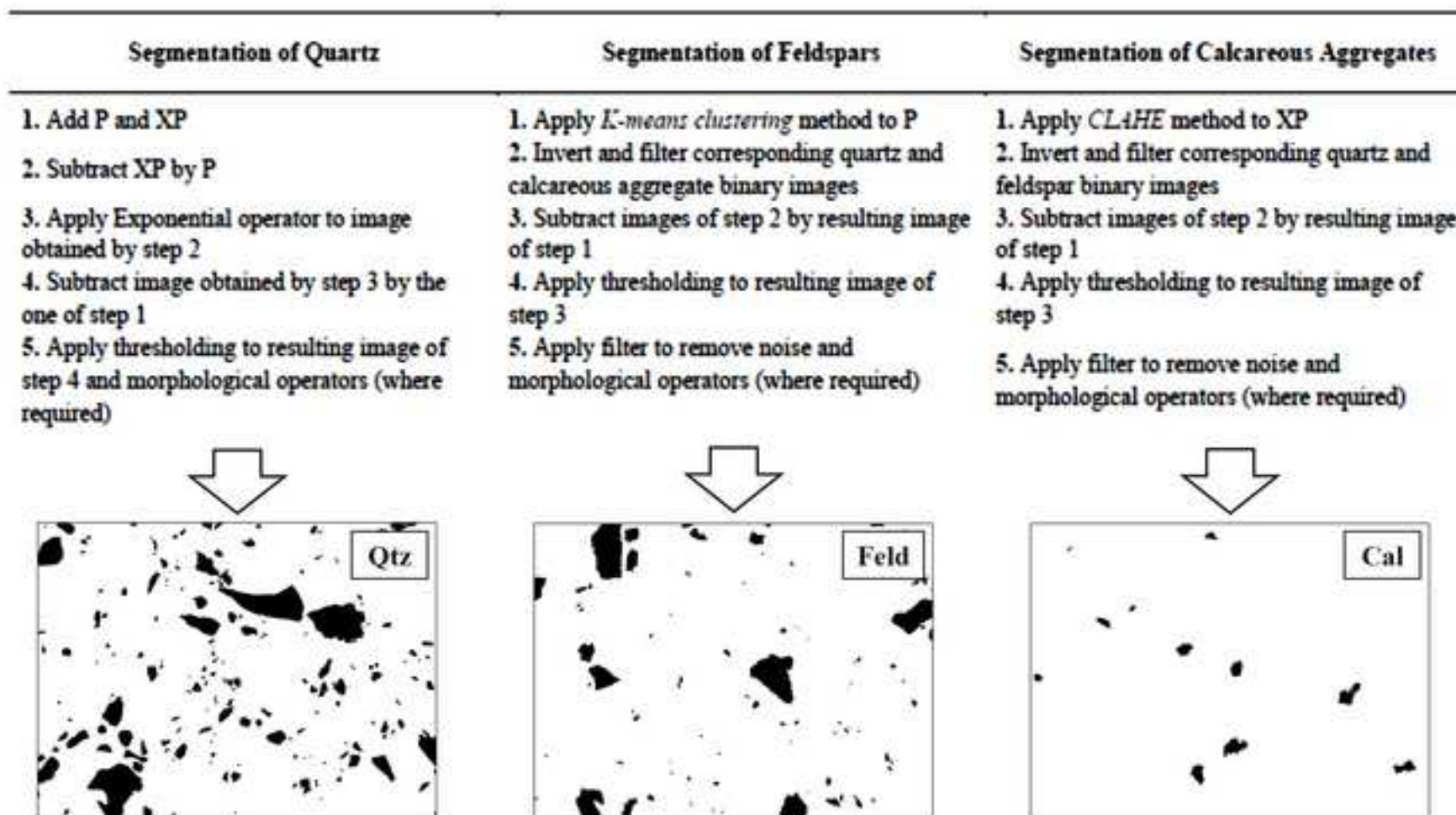
Figure 9

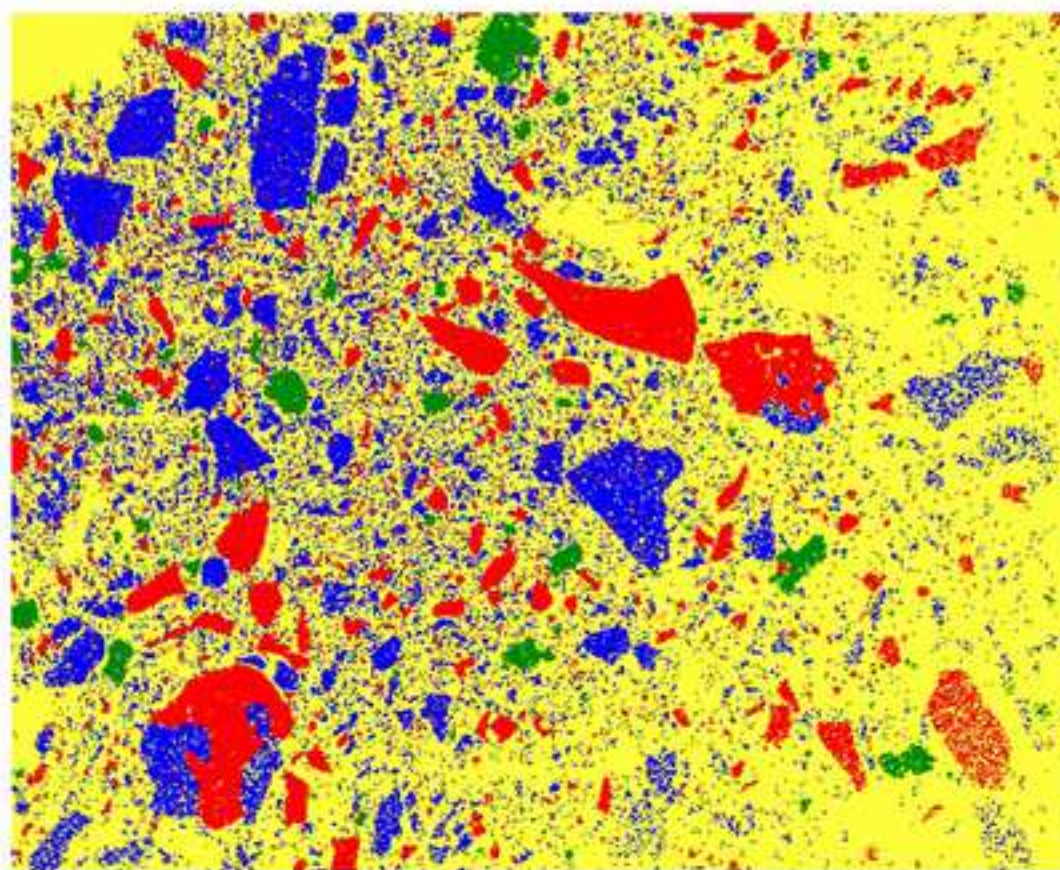












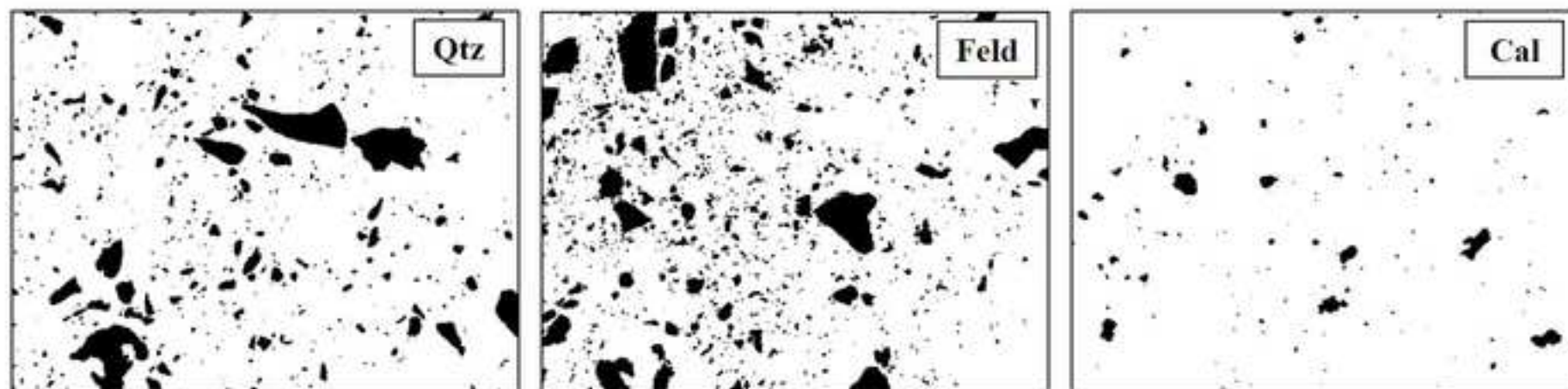
Quartz

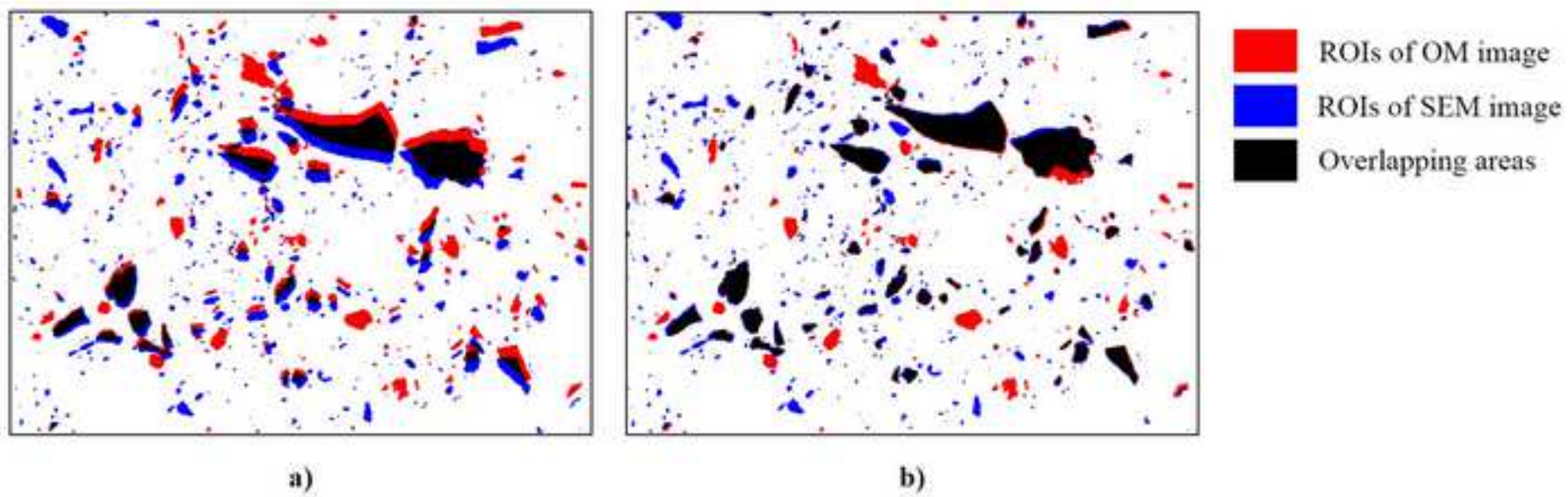


Feldspars



Calcareous Aggregates





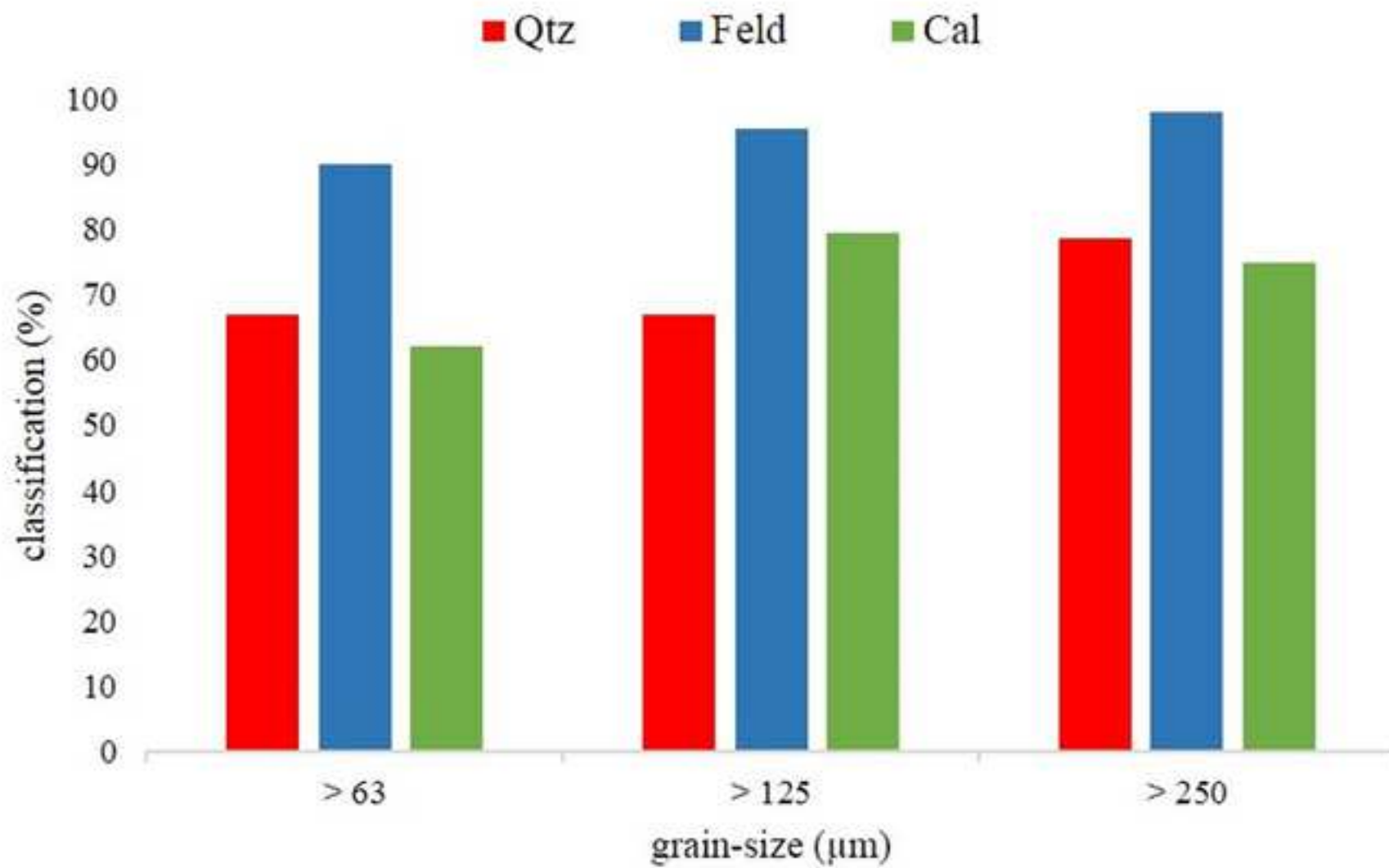


Table 1

	TK66			TK69		
	Qz	Feld	Cal	Qz	Feld	Cal
total points	823	334	43	879	156	165
mean	205.8	83.5	10.8	219.8	39.1	41.3
SD	15.6	12.2	21.1	39.1	29.5	32.7
RSD	0.1	0.8	0.3	0.2	2.8	0.8
percentage	68.6	27.8	3.6	73.3	13.0	13.8

Table 2

	grain size (m)	TK66		TK69		TK66		TK69	
		OM	%	SEM	%	OM	%	SEM	%
Quartz	16-32	148	20.11	612	46.43	196	23.61	636	48.48
	32-63	269	36.55	381	28.91	321	38.67	396	30.18
	63-125	206	27.99	238	18.06	234	28.19	206	15.70
	125-250	88	11.96	68	5.16	60	7.23	54	4.12
	250-500	20	2.72	14	1.06	14	1.69	15	1.14
	>500	5	0.68	5	0.38	5	0.60	5	0.38
	TOT	736		1318		830		1312	
Feldspars	16-32	70	23.81	1311	48.63	329	51.17	1181	51.89
	32-63	83	28.23	862	31.97	234	36.39	719	31.59
	63-125	82	27.89	359	13.32	61	9.49	290	12.74
	125-250	42	14.29	134	4.97	14	2.18	56	2.46
	250-500	14	4.76	27	1.00	5	0.78	22	0.97
	>500	3	1.02	3	0.11	0	0.00	8	0.35
	TOT	294		2696		643		2276	
Calcite aggregates	16-32	0	0.00	199	58.70	74	37.37	42	53.85
	32-63	7	17.50	88	25.96	80	40.40	18	23.08
	63-125	11	27.50	18	5.31	34	17.17	9	11.54
	125-250	18	45.00	26	7.67	6	3.03	6	7.69
	250-500	4	10.00	7	2.06	2	1.01	1	1.28
	>500	0	0.00	1	0.29	2	1.01	2	2.56
	TOT	40		339		198		78	

Table 3

Grain size (μm)	Qtz		Feld		Cal	
	N	M	N	M	N	M
> 63	586	632	915	241	73	78
> 125	157	192	268	102	35	33
> 250	41	44	63	46	6	9